

A Morphology Map Based on Phase Evolution in Polymer Blend Films

Hyun-joong Chung,[†] Howard Wang,[‡] and Russell J. Composto^{*,†}

Department of Materials Science and Engineering and Laboratory for Research on the Structure of Matter, University of Pennsylvania, Philadelphia, Pennsylvania 19104-6272, and Department of Materials Science and Engineering, Michigan Technological University, Houghton, Michigan 49931

Received July 12, 2005; Revised Manuscript Received October 27, 2005

ABSTRACT: We present a novel morphology map based on pattern development mechanisms in polymer blend films. Six distinct mechanisms are found for poly(methyl methacrylate) (PMMA):poly(styrene-*ran*-acrylonitrile) (SAN) films for thickness values and bulk compositions between 50–1000 nm and $\phi_{\text{PMMA}} = 0.3$ –0.8, respectively. In regime A ($\phi_{\text{PMMA}} = 0.3$), PMMA is completely depleted from the midlayer by preferential wetting, resulting in a stable PMMA/SAN/PMMA trilayer. With increasing ϕ_{PMMA} (0.4–0.7), pattern development is driven by phase separation in the midlayer, which produces circular domains, irregular domains, and bicontinuous patterns denoted as regimes B, C, and D, respectively. Here, shape factors are used for the first time to quantitatively distinguish these regimes. In regime E ($\phi_{\text{PMMA}} = 0.8$), the SAN phase is the minority component in the midlayer and breaks up into droplets in a smooth PMMA film. In regime F ($\phi_{\text{PMMA}} = 0.4$ or 0.5; $d < 80$ nm), films initially develop a trilayer structure, which then ruptures upon dewetting of the SAN midlayer. Trilayer stability is analyzed using a free energy model that attributes dewetting to capillary fluctuations at the PMMA/SAN interface. This study of pattern development mechanisms will serve as a guideline to control morphology shape and feature size, which are both critical design parameters for technological applications such as organic devices and membranes.

1. Introduction

Polymer films in applications ranging from tissue scaffolds to electrooptical devices typically contain multiple polymer types and, sometimes, inorganic particles. Optimizing the performance of such films requires a fundamental understanding of film morphology and stability. By controlling feature size in thin film blends, patterns produced by controlled phase separation have the potential to replace conventional lithographic methods to create mesoscale structures from tens of nanometers to tens of microns. Because most polymer blends are incompatible, films undergo phase separation in the presence of a hard wall and free surface (i.e., confinement). Wetting at these interfaces can dominate the morphology evolution because of the large surface-to-volume ratio in thin films.¹ Films can also become destabilized by capillary fluctuations caused by long-range van der Waals forces and/or compositional inhomogeneity.² Previous studies^{3–25} reveal that phase separation in binary polymer films can produce smooth or rough surfaces, bicontinuous or discrete patterns, and stratified or perforated layers, depending on experimental conditions. Although several types of arresting morphologies have been produced, rules governing the regulation of pattern development and morphology are not yet available. To provide guidelines for producing a desired structure, this paper presents a novel phase map that delineates morphologies according to the mechanism underlying pattern development rather than the postmortem structure.

Upon annealing in the two-phase region, a three-stage morphological pathway has been identified for poly(methyl methacrylate) (PMMA):poly(styrene-*ran*-acrylonitrile) (SAN) blends at the “bulk” critical composition (50:50) and film

thickness range of 100–1500 nm.^{8,9} Upon spin-coating and drying, this blend is homogeneous, allowing for a thermodynamically stable, well-defined initial state. During the early stage of phase evolution, PMMA wets both the free surface and substrate via hydrodynamic-driven wetting through 3D bicontinuous “tubes” generated by spinodal decomposition.²⁶ The intermediate stage is identified by pseudo-2D growth of PMMA-rich (denoted PMMA) domains that span the SAN-rich (denoted SAN) midlayer.⁸ This growth scales with time and thickness as $t^{1/3}$ and $d^{2/3}$, respectively, in agreement with a coalescence model.¹⁴ In the late stage, the PMMA/PMMA:SAN/PMMA structure formed by the end of the intermediate stage ruptures due to interfacial fluctuations that eventually produce a rough film containing SAN droplets encapsulated by PMMA wetting layers.^{10,11} For films less than $d = 100$ nm but greater than the radius of gyration (R_g), a PMMA/SAN/PMMA trilayer is formed prior to the dewetting of the sandwiched SAN layer.¹²

In this paper, we construct a morphology map of the intermediate stage morphology by identifying the dominant pattern development mechanism within a window of blend composition and film thickness. To date, studies have reported various patterns depending on blend composition^{5,13,15,22} and film thickness.^{12,13,16} However, a comprehensive understanding is lacking because an understanding of pattern development requires knowledge of the growth mechanism as well as the time range over which this mechanism dominates. Building upon prior studies at a PMMA volume fraction, ϕ_{PMMA} , of 0.5, the present study aims to identify the pattern evolution mechanisms for PMMA:SAN blends ranging from $d = 50$ to 1000 nm and $\phi_{\text{PMMA}} = 0.3$ to 0.8. Specifically, by analyzing the shape factor (SF), number-average domain diameter, and correlation length, six distinct mechanisms are identified over a well-defined window of composition and thickness. For $d > 80$ nm, discrete ($SF > 0.8$), irregular ($0.4 < SF < 0.8$), and bicontinuous ($SF < 0.4$) domains of PMMA and SAN are generated with

[†] University of Pennsylvania.

[‡] Michigan Technological University.

* To whom correspondence should be addressed: Ph (215) 898-4451; Fax (215) 573-2128; e-mail composto@lrsm.upenn.edu.

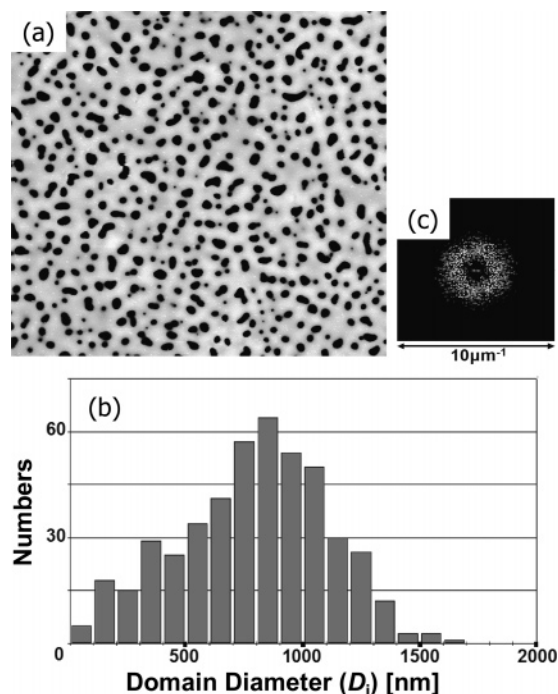


Figure 1. An example of pattern analysis for a PMMA:SAN film with $d = 470$ nm and $\phi_{\text{PMMA}} = 0.4$, after $t = 24$ h. (a) Unprocessed AFM image ($40 \times 40 \mu\text{m}^2$) of the interface topography of SAN (light) after removing PMMA (dark). After converting this image into black and white by defining a threshold gray value, the PMMA area fraction (A_d) and shape factor (SF) can be determined as well as the PMMA domain diameter distribution, which is shown in (b). The number-average domain diameter (\bar{D}_n) is determined from (b). The fast Fourier transform of (a) is shown in (c) and used to determine the correlation length (ξ). For this particular sample, the morphology is quantified by $A_d = 16.6\%$, $SF = 0.83$, $\bar{D}_n = 785$ nm, and $\xi = 2380$ nm.

increasing PMMA composition. For $d < 80$ nm, a trilayer structure is initially formed, followed by dewetting of the SAN midlayer. On the basis of this morphology map, a criterion to generate a stable PMMA/SAN/PMMA structure by a one-step fabrication process is proposed as a novel route to create trilayer structures for device applications.

The rest of this article is organized as follows. In section 2, sample preparation and the image analysis method are presented. Section 3.1 summarizes the six regimes of pattern development with a morphology map. In section 3.2, pattern development kinetics is presented for regimes where $\phi_{\text{PMMA}} = 0.4$ – 0.7 and $d > 80$ nm. In section 3.3, the stability of transient PMMA/SAN/PMMA trilayer structure is discussed. Section 3.4 comments on our current understanding, remaining questions, and future directions in polymer blend films. The potential impact for improving upon polymeric devices is also discussed. Finally, section 4 summarizes this article.

2. Experimental Methods

Sample Preparation. The weight-average molecular weights and polydispersities of PMMA and SAN (33 wt % AN) are 82.5K and 1.05 and 118K and 2.24, respectively. This blend displays lower critical solution behavior with a critical temperature of ~ 160 °C. At 185 °C, the coexisting compositions are nearly pure PMMA and SAN.²⁷ Thus, instead of PMMA-rich and SAN-rich, we simplify the nomenclature to PMMA and SAN, respectively. For substrates, silicon wafers were first washed with hydrofluoric acid to remove the native oxide before a fresh oxide layer (~ 2 nm) was grown in a UV-ozone chamber. Polymer blends with bulk compositions $0.3 \leq \phi_{\text{PMMA}} \leq 0.8$ were dissolved in methyl isobutyl ketone, spin-cast on silicon wafers, and then dried at 120 °C in a vacuum for

24 h. Films were smooth (root-mean-square roughness < 0.3 nm) and homogeneous. The ellipsometric film thickness (d) ranged from 50 to 1000 nm. Samples were annealed on a hot stage (Mettler FP-82, Mettler Toledo, Inc.) at 185 °C in argon up to 72 h. Surface and internal morphologies were investigated using a Dimension 3000 AFM (Digital Instrument, Inc.) driven in Tapping Mode. To reveal the internal PMMA/SAN interface morphologies, the PMMA phase was selectively removed by first exposing to radiation, either UV radiation in an ozone atmosphere or 2 MeV He^+ ($\sim 2 \mu\text{C}$), followed by immersing in acetic acid.

Image Analysis. Quantitative image analysis of the morphology was performed to distinguish between different regimes of pattern development. Whereas most studies have used a qualitative approach, Budkowski and co-workers quantified the area fraction, domain shape, and connectivity by using so-called Minkowski measures.¹⁸ One limitation is that these measures do not provide the domain size and is therefore an insufficient analysis method for following domain growth kinetics.

In our study, we analyze the shape, via the PMMA area fraction (A_d) and shape factor (SF), as well as the size, via the number-average domain diameter (\bar{D}_n) and correlation length between domains (ξ), to elucidate the pattern development mechanism. For example, the image analysis procedure is demonstrated in Figure 1, which shows the internal (interfacial) morphology of a film with $d = 470$ nm and $\phi_{\text{PMMA}} = 0.4$ film after 24 h. First, the topography of the interface (i.e., SAN) is mapped, and the relative height is displayed in a gray scale, as shown in Figure 1a. PMMA domains that span two wetting layers at the surface and the substrate were removed. Thus, the dark circular regions correspond to the removed PMMA (i.e., exposed substrate). By setting a threshold gray scale (i.e., height) at the mean value of the surface and the substrate peaks, Figure 1a was converted to black, the PMMA domains, and white, the SAN matrix. In this study, A_d , SF , and \bar{D}_n were determined using Image Processing Tool Kit (v4.0, Reindeer Graphics, Inc.).²⁸ A_d was simply measured by quantifying the area fraction of PMMA domains over a $40 \mu\text{m} \times 40 \mu\text{m}$ scan area. This area was varied between samples to ensure a statistically significant sampling of the number of domains. The SF is described by

$$SF = \frac{\sum_i A_i \frac{4\pi A_i}{P_i^2}}{\sum_i A_i} \quad (1)$$

where A_i and P_i are the area and the perimeter of an individual domain.²⁹ The SF ranges from 0 to 1 for a line and circle, respectively. The domain diameter D_i is defined as the diameter of a circle of area A_i . The D_i distribution is plotted in Figure 1b is used to determine \bar{D}_n

$$\bar{D}_n = \frac{\sum_i D_i}{N} \quad (2)$$

where N is the total number of domains. Finally, the correlation length between domains (ξ) was obtained by taking a fast Fourier transform (FFT) using the Nanoscope III software (v5.12, Digital Instrument, Inc.). By definition, ξ is defined as

$$\xi(t) = \frac{2\pi \int S(k,t) dk}{\int k S(k,t) dk} \quad (3)$$

where $S(k,t)$ is the density autocorrelator and k is the wavevector.³⁰ For simplicity, the correlation length is determined from the dominant wavevector, $k_{\text{max}}(t)$, so that $\xi(t) = 2\pi/k_{\text{max}}(t)$. Figure 1c shows the FFT taken from the internal morphology in Figure 1a.

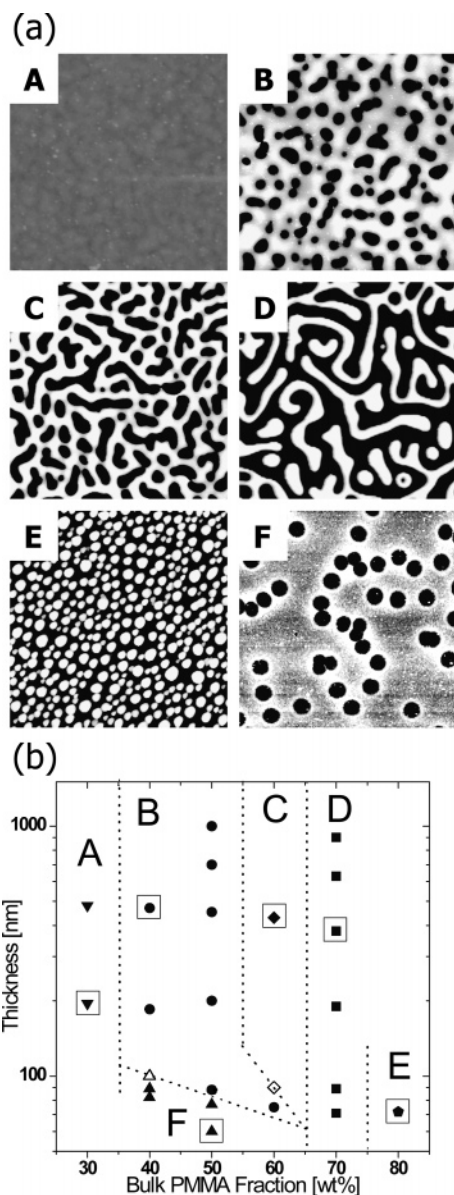


Figure 2. (a) Representative interface patterns of six distinct pattern evolution mechanisms during the intermediate stage and (b) a morphology map keyed to these patterns over a range of d and ϕ_{PMMMA} . The AFM images in (a) show the PMMA (dark) and SAN (light) phases in the midlayer. The six patterns are characterized by (A) a smooth, stable midlayer (up to 72 h), (B) discrete, circular domains of PMMA ($SF > 0.8$), (C) discrete, irregular domains of PMMA ($0.4 < SF < 0.8$), (D) bicontinuous PMMA and SAN domains ($SF < 0.4$), (E) droplets of PMMA, and (F) a roughened, dewetted midlayer. Annealing times are (A, B, C, and D) 24 h, (E) 12 h, and (F) 8 h. The images in (a) correspond to the large open squares in (b). The small open symbols represent a crossover regime where two patterns are observed across the same samples.

3. Results and Discussion

3.1. Morphology Map: Overview of Regimes. During the intermediate stage, PMMA:SAN films are found to exhibit six distinct pattern development pathways over a range of thickness, $d = 50\text{--}1000$ nm, and PMMA volume fraction, $\phi_{\text{PMMMA}} = 0.3\text{--}0.8$. Figure 2a shows AFM images of six internal morphologies, which represent regimes A, B, C, D, E, and F. Figure 2b displays these regimes in terms of a “morphology map” which shows the range of d and ϕ_{PMMMA} for each unique morphology mechanism. In regime A (i.e., very PMMA poor), the PMMA phase is completely depleted from the midlayer after wetting the surface and substrate. Consequently, a smooth SAN midlayer

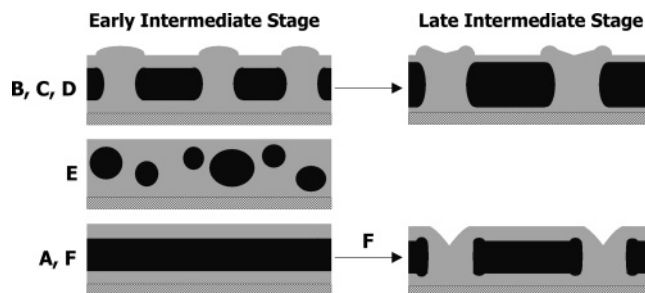


Figure 3. Cartoons of the film cross section corresponding to regimes B, C, and D (top), regime E (middle), and regimes A and F (bottom) during the early (left) and late (right) intermediate stages (IS). Black and gray correspond to SAN and PMMA phases, respectively. In regimes B, C, and D, surface hills form at the beginning of the IS and then collapse during the later part of the IS. In all three cases, the collapse correlates with pattern evolution in the midlayer. In regime E, the blend has insufficient SAN to form a continuous stable midlayer, and therefore the SAN breaks into droplets dispersed in a PMMA matrix. In regime A, the trilayer structure that forms during the early IS is stable, whereas in regime F the trilayer becomes unstable during the late IS because of midlayer dewetting as shown on the right. See text for details.

is observed after the removal of PMMA, as noted in panel A of Figure 2a. With increasing ϕ_{PMMMA} , $0.4\text{--}0.7$, a pseudo-2D phase separation mechanism dictates pattern development in the midlayer for $d > 100$ nm. This behavior produces regimes B, C, and D, which are characterized by circular domains, elongated domains, and bicontinuous patterns, respectively. The shape factor provides a quantitative method to discern the regimes, $SF_B > 0.8$, $0.4 < SF_C < 0.8$, and $SF_D < 0.4$, respectively. In regime E where $\phi_{\text{PMMMA}} = 0.8$ (i.e., very SAN poor), the SAN phase becomes a minority component in the midlayer, is unable to form a continuous matrix, and thus breaks up into individual domains as noted in panel E of Figure 2a. Regime F (i.e., very thin) is characterized by circular domains of PMMA with a nearly monodisperse domain distribution, as shown in panel F of Figure 2a. Although they appear similar to panel B in Figure 2a, these domains result from an entirely different mechanism, namely a dewetting of SAN midlayer from the PMMA wetting layers, as discussed in section 3.3.

For regimes A–F, Figure 3 shows cartoons of the cross-sectional morphologies during the early and late intermediate stages. At the beginning of the intermediate stage, films in regimes B, C, and D exhibit a trilayer structure, air/PMMA/SAN:PMMA/PMMA/substrate, with PMMA-rich domains that span the wetting layers. The hydrodynamic flow of PMMA toward the surface during the early stage produces surface hills over the PMMA-rich domains in the midlayer. Later, the hills collapse due to a reversal of the pressure distribution,⁹ as discussed in section 3.2. In regime E, the SAN volume fraction is too low to form a stable midlayer, and therefore SAN domains form within a stable film of PMMA. In this regime, SAN droplet growth is extremely slow, probably because SAN diffuses slowly through the PMMA matrix and has limited solubility in PMMA. In contrast to all other regimes, the surface remains smooth throughout the intermediate stage. In regimes A and F, both types of films initially form a PMMA/SAN/PMMA trilayer. However, if films are thin (< 80 nm), the SAN layer dewets from the top and bottom PMMA layers, resulting in surface dimples characteristic of regime F, as discussed in section 3.3.

3.2. Pseudo-2D Phase Separation (Regimes B, C, and D). During the intermediate stage, the patterns in regimes B, C, and D are characterized by discrete domains of PMMA, irregular/elongated domains of PMMA, and bicontinuous PMMA and SAN domains, respectively. In this section, the surface and

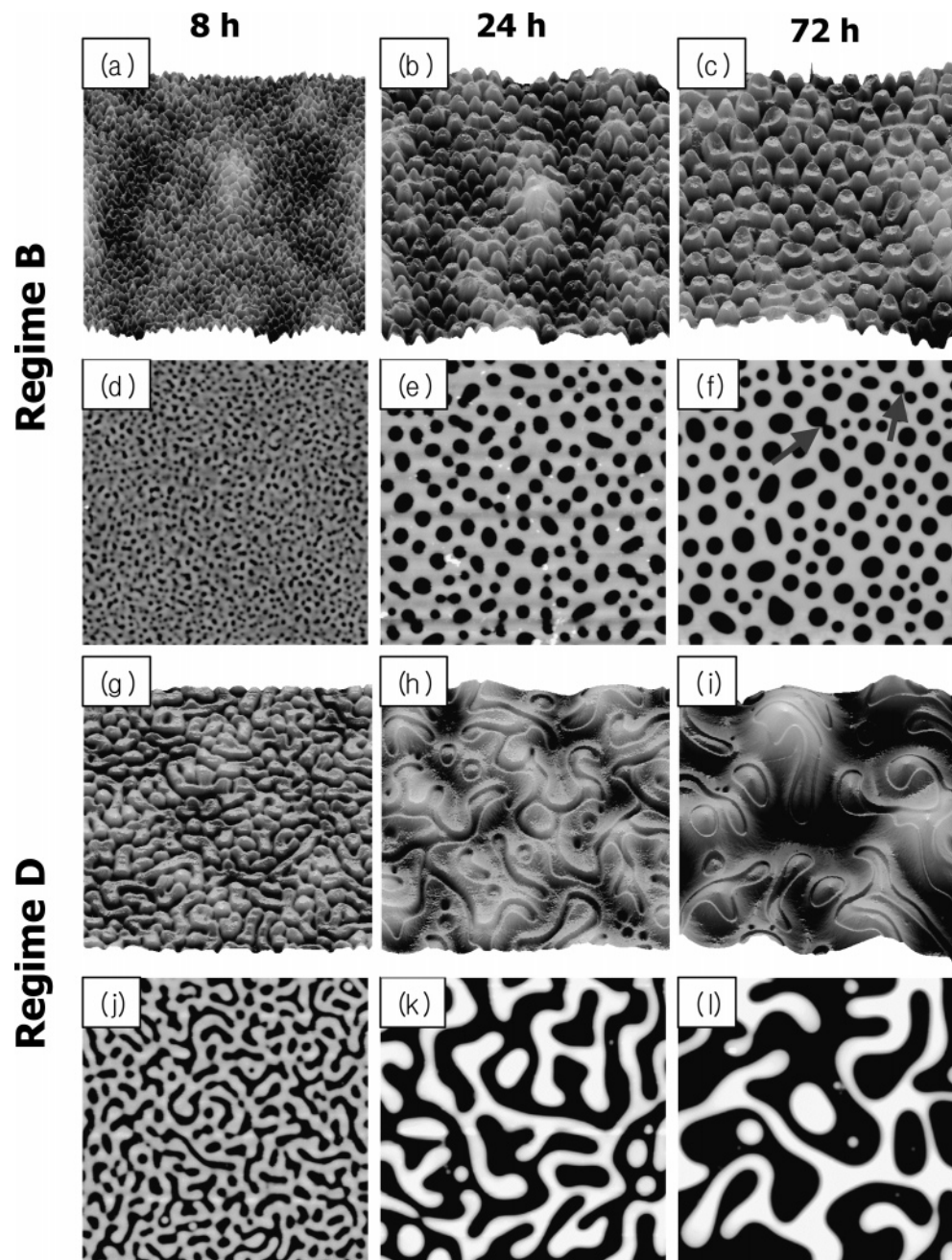


Figure 4. Surface (a, b, c, g, h, i) and interface (d, e, f, j, k, l) patterns in regime B (a–f; $d = 1000$ nm, $\phi_{\text{PMMA}} = 0.5$) and regime D (g–l; $d = 900$ nm, $\phi_{\text{PMMA}} = 0.7$). To enhance fluctuations over the range of length scales, surface images are represented by 3D projections with z ranges of ± 50 nm (a–c) and ± 150 nm (g–i). All interface images have a z range of ± 300 nm. Annealing times are 8 h (a, d, g, j), 24 h (b, e, h, k), and 72 h (c, f, i, l). Arrows in (f) denote coalescing domains. All scans are $40 \times 40 \mu\text{m}^2$.

the interface patterns are presented. The growth mechanism describing pattern evolution is determined by the composition of the midlayer PMMA composition, quantified by A_0 . This parameter is used to explain the pattern evolution in regimes B and D as well as the pattern transition unique to regime C. In regime B, analysis of ξ and \bar{D}_n leads to a scaling model for predicting pattern size as a function of d and t .

For regimes B and D, the morphology evolution is shown in Figure 4a–f and Figure 4g–l, respectively. AFM images of the surface and interface morphologies were taken after 8, 24, and 72 h, which is within the intermediate stage. Figure 4a–c and Figure 4g–i show the surface as a 3D projection in order to discern short- and long-wavelength variations in pattern height. Here, the light and dark colors represent high and low regions, respectively; the height scales, given in the caption,

are exaggerated to accentuate the surface patterns. Interface morphologies in Figure 4d–f and Figure 4j–l are shown in 2D projection to highlight the lateral pattern. Here, dark and light correspond to the PMMA-rich domains and midlayer SAN-rich phases, respectively.

For regime B, the pattern evolution of the surface and interface are shown in Figure 4a–c and Figure 4d–f, respectively. After 8 h, small hills are seen in Figure 4a. These hills appear during the early stage in response to the hydrodynamic flow of PMMA toward the surface.²⁶ The height and diameter of the hills grow with time as shown in Figure 4b. Figure 4c shows that the tops of the hills collapse after 72 h. As explained in an earlier paper,⁹ the hill implosion results from a reversal of the pressure gradient that drives PMMA from the surface into the PMMA domains in the midlayer. Figure 4a–c also

shows that long-wavelength fluctuations appear during the intermediate stage with wavelength values of 16, 20, and 27 μm , respectively. The root-mean-square (rms) roughness increases as 5.0, 8.3, and 10.3 nm, respectively. We have previously shown that the growth of these long-wavelength fluctuations eventually leads to film rupture during the late stage.¹⁰ Interface images in Figure 4d–f show that the discrete PMMA domains grow monotonically, a characteristic of the intermediate stage.⁹ A comparison of the surface hills in Figure 4a–c and the PMMA domains in Figure 4d–f shows that they have similar diameters and spacing. This observation suggests that the surface morphology reflects the internal pattern evolution and provides support that AFM imaging of the surface can be used to follow phase separation taking place in the midlayer (cf. Figure 3, regimes B–D).

In contrast to regime B, the morphology of regime D shows a highly interconnected pattern as noted by the surface and interface images in Figure 4g–i and Figure 4j–l, respectively. After 8 h, Figure 4g shows elongated and irregular-shaped mounds that appear on the surface. These surface mounds form for the same reason as the hills in Figure 4a, namely, to relieve pressure due to material flow from the bulk to surface. Upon further annealing, however, continuous valleys are observed at the surface as shown in Figure 4h,i. This morphological transition from surface mounds to valleys has not been observed before this study. Similar to regime B, long-wavelength fluctuations appear on the surface and show an increasing wavelength and amplitude. After 8, 24, and 72 h, the wavelengths increase as 13, 21, and 27 μm , respectively. The rms roughness values also increase monotonically as 7.7, 13.4, and 41.7 nm, respectively. Similar to regime B, these long-range fluctuations are responsible for film rupture. After 8 h, Figure 4j shows that the interface pattern has irregular-shaped PMMA domains in a continuous SAN matrix. After 24 and 72 h, the interface patterns show bicontinuous PMMA and SAN domains that coarsen as in parts k and l of Figure 4, respectively.

The key to understanding the morphological patterns characteristic of regimes B–D is to analyze the midlayer composition. In the theory of 2D spinodal decomposition, discrete and bicontinuous patterns are expected at off-critical and critical compositions, respectively.^{30–33} As shown in Figure 3, PMMA wetting at the air and substrate reduces the PMMA concentration in the midlayer relative to the bulk value. This depletion of PMMA explains why bicontinuous patterns are observed at $\phi_{\text{PMMA}} = 0.7$ (i.e., regime D). In our study, the PMMA composition in the midlayer is represented by A_d . In Figure 5, A_d is plotted vs t for bulk ϕ_{PMMA} values of 0.5 (open symbols), 0.6 (half-filled symbols), and 0.7 (filled symbols), corresponding to regimes B, C, and D, respectively. In regime B, A_d initially increases with time and then approaches $\sim 28\%$. In contrast, in regime D A_d approaches $\sim 50\%$, the critical composition. Interestingly, the plateau values are insensitive to d , suggesting that the wetting layer thickness values are proportional to d . For regime C, A_d increases very strongly, from 13% to $\sim 40\%$ between 2 and 24 h, respectively. This behavior explains why the pattern transitions from circular ($SF = 0.75$) to irregular ($SF = 0.55$), as shown in panel C of Figure 2a. In short, A_d accurately predicts pattern evolution and transitions in polymer blend films during the intermediate stage of phase separation.

Understanding pattern development in polymer blend films requires analysis of growth kinetics. In classical theories of spinodal decomposition, dynamic scaling hypothesis predicts that domain growth scales as $\xi(t) \sim t^\alpha$, where the growth exponent α depends on the mechanism.³⁴ For bulk polymer

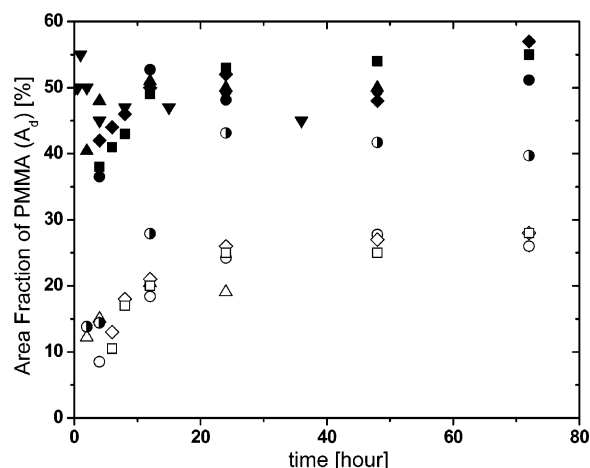


Figure 5. Area fraction of PMMA domains (A_d) as a function of annealing time (t) for regimes B (open symbols), C (half-filled symbols), and D (filled symbols). In regimes B and D, A_d values approach 0.28 and 0.5, respectively, whereas in regime C, A_d increases from 0.1 to 0.4. The symbols denote thickness values from Figure 6. For d values from ~ 100 to 1000 nm, A_d is independent of thickness.

blends, discrete droplet domains grow by diffusion or domain coalescence at off-critical compositions and scale as $t^{1/3}$.^{35–38} On the other hand, bicontinuous patterns grow more quickly, as t^1 , because of a hydrodynamic pumping mechanism triggered by minority phase percolation at critical compositions.³⁸ To apply dynamic scaling to polymer blend films, two conditions must be satisfied. First, patterns should grow proportional to size, while retaining their shape and periodicity.³⁴ In our study, the SF values in regimes B and D are nearly invariant at ~ 0.85 and ~ 0.35 , respectively. Second, the midlayer PMMA composition (i.e., A_d) should remain constant during phase separation, as pointed out by Haas and Torkelson.³⁹ In Figure 5, A_d values in regime B increase from 0.1 to 0.28 during the intermediate stage whereas regime D also shows a slight increase from 0.4 and 0.6. Although not strictly invariant, these values likely remain within the off-critical and critical portion of phase diagram, respectively. Therefore, the dynamic scaling hypothesis can be used to analyze the growth mechanisms observed in regimes B and D.

In regime B, a previous study shows that the pattern growth is due to the coalescence of discrete PMMA domains, as noted by arrows in Figure 4f.¹⁴ In this mechanism, originally proposed by Tanaka,⁴⁰ the SAN domains between adjacent PMMA domains behave like tubes squeezed by the surrounding PMMA domains which are connected via the two wetting layers. In this approach, a scaling law for the growth of discrete domains observed in regime B is given by¹⁴

$$\xi \sim (\sigma/\eta)^{1/3} d^{2/3} t^{1/3} \quad (4)$$

where σ and η are the interfacial tension between PMMA and SAN phases and the viscosity of PMMA, respectively. This scaling model was also recently used to explain the slowing down of domain growth in polymer blend films containing nanoparticles, where η increases with nanoparticle content.⁴¹ Figure 6a shows the $\xi \sim t^{1/3}$ relation for various d , consistent with the scaling prediction in eq 4. Note, the scaling relationship $\xi \sim d^{2/3}$ was also demonstrated in a previous study.¹⁴

In regime D, ξ scales as t^α where α decreases from 0.62 to 0.28 as d decreases from 900 to 90 nm, as shown in Figure 6b. Whereas a hydrodynamic pumping mechanism predicts $\xi \sim t$ for bicontinuous patterns, plotting ξ against $t^{1/3}$ and t demonstrates that pattern growth does not follow either growth law

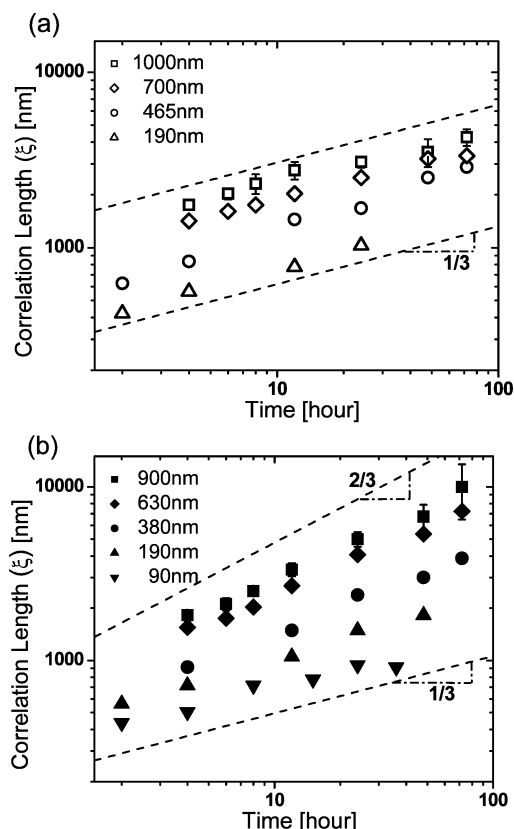


Figure 6. Correlation length (ξ) vs time (t) for regimes B (a) and D (b), where $\phi_{\text{PMMA}} = 0.5$ and 0.7 , respectively. Broken lines are to guide the eye. In regime B, pattern growth scales as $\xi \sim t^{1/3}$, consistent with a coalescence model. In regime D, the growth exponent decreases from 0.62 to 0.28 as d decreases from 900 to 90 nm, suggesting that hydrodynamic flow is suppressed by film confinement.

and suggests that hydrodynamic pumping is suppressed with increasing confinement (i.e., decreasing d). This suppressed flow may result from an increase in the elasticity of entangled chains caused by confinement.¹⁴ Alternatively, suppression may result from the large curvature associated with confining the bicontinuous pattern shown in Figure 4k,l. Van der Linden and co-workers⁴² showed that the interfacial tension of curved domains increases strongly as the radius of curvature decreases, namely $\sigma \sim r^{-2}$. Because r scales with ξ , the slowing down of pattern growth, as shown in Figure 6b, is in qualitative agreement with suppression due to an increase in σ as d decreases.

Finally, for the circular domains characteristic of regime B, \overline{D}_n is the appropriate measure of growth kinetics. For $\phi_{\text{PMMA}} = 0.5$, Figure 7 shows how \overline{D}_n varies as a function of both d and t . In agreement with eq 4, \overline{D}_n obeys the power law relationship $d^{2/3}t^{1/3}$. Thus, controlling pattern size in regime B is best achieved by varying d . For example, \overline{D}_n increases from 140 to 260 nm between 0.5 and 15 h and from 1200 to 2300 nm between 12 and 72 h for $d = 90$ and 1000 nm, respectively. Note, for the thinnest films, $d = 90$ nm (down triangles) and 190 nm (up triangles), the intermediate stage ends after only 15 and 24 h, respectively, before films rupture. On the other hand, for the thickest films, $d = 465$ nm (circles), 700 nm (lozenges), and 1000 nm (squares), the intermediate stage extends beyond 72 h, suggesting that \overline{D}_n values larger than 1500 , 1750 , and 2300 nm are accessible at longer annealing times. In conclusion, the quantitative analysis of pattern evolution in regimes B and D provides an important guideline for preparing discrete and bicontinuous patterns over a wide range of feature sizes.

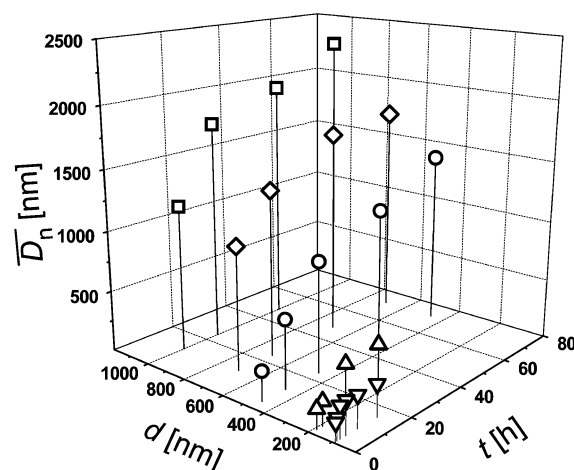


Figure 7. Number-average domain diameter (\overline{D}_n) as a function of annealing time (t) and film thickness (d) in regime B ($\phi_{\text{PMMA}} = 0.5$).

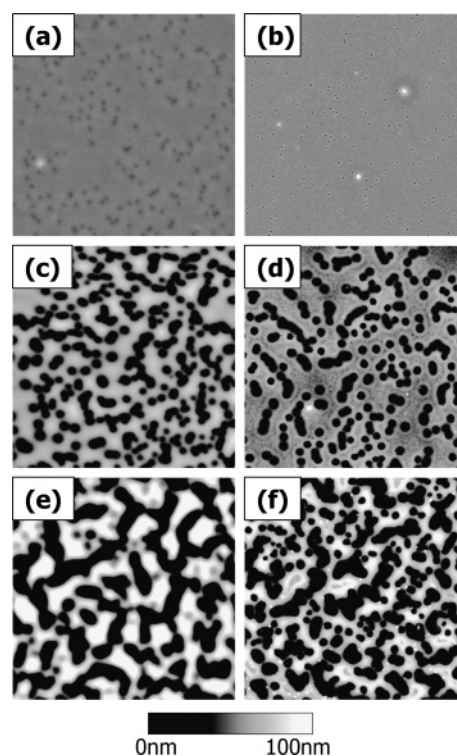


Figure 8. AFM images of the surface (a, c, e) and interface (b, d, f) of an SAN:PMMA film ($d = 75$ nm, $\phi_{\text{PMMA}} = 0.5$) characteristic of regime F after 2 h (a, b), 12 h (c, d), and 24 h (e, f). Surface depressions (a, c, e) and midlayer holes (b, d, f) grow with time, coalesce, and then rupture the film. This roughening mechanism is distinct from that of regimes B, C, and D.

3.3. Dewetting in Trilayer Structures (Regimes A and F).

Regimes A and F cover regions of the morphology map in Figure 2 corresponding to PMMA-rich, $\phi_{\text{PMMA}} = 0.3$, and very thin, $d < 100$ nm, respectively. In both regimes, films initially form a laterally homogeneous trilayer structure of PMMA/SAN/PMMA as shown in Figure 3. In this section, we focus first on the pattern development in regime F and then analyze trilayer stability using spinodal dewetting theory. Figure 8 shows the surface (left) and interface (right) pattern development of a 75 nm film with $\phi_{\text{PMMA}} = 0.5$. After 2 h, depressions and holes appear on a smooth surface and interface as noted in parts a and b of Figure 8, respectively. Although taken from different areas, these images show that the holes and dimples have a similar number density and size, suggesting that they nucleate

at similar times throughout the film. After 12 h, the dimples and holes grow in size and coalesce, resulting in the necklace of connected features shown in parts c and d of Figure 8. After 24 h, long strings of depressions and holes form (cf. parts e and f of Figure 8, respectively) and the film ruptures. Afterward (not shown), the film becomes macroscopically rough with droplets of SAN encapsulated by a wetting layer of PMMA.¹²

Although the final, roughened morphology characteristic of regime F is indistinguishable from regime B (cf. Figure 2k,l in ref 9), the intermediate stage pattern development in regime F follows an entirely different pathway. First, a comparison of the surface images in Figures 4a–c and 8a,c,e shows that the surface of regime B is dominated by hills whereas regime F shows depressions. Second, the interface images display circular features in both regimes (Figure 4d–f and Figure 8b). However, once they collide, holes do not relax back to a round shape in regime F and are able to maintain the high interfacial area shown in Figure 8d. Third, in regime F, ξ is $\sim 3 \mu\text{m}$ for $d = 75 \text{ nm}$ and invariant with time (Figure 8b,d), whereas in regime B, ξ increases from 260 to 650 nm between 0.5 and 15 h at a similar thickness, 90 nm. On the basis of these distinct differences, regimes B and F were mapped onto Figure 2b with a transition thickness of around 80 nm.

One can hypothesize that the holes in Figure 8b,d,f and surface depressions in Figure 8a,c,e originate from the dewetting of the middle SAN layer from PMMA wetting layers as sketched in Figure 3 (left bottom). To test this hypothesis, we performed control experiments with a trilayer of PMMA (100 nm)/SAN (20 or 160 nm)/PMMA (100 nm) on silicon at 185 °C in a vacuum. For trilayers with an SAN midlayer of 20 nm (i.e., similar to regime F), surfaces were initially smooth for 3 h, but then periodic dimples ($\xi = 400 \text{ nm}$) across the surface appeared after 4 h. On the other hand, for a midlayer of 160 nm (i.e., comparable to regime A samples), films remained smooth even after 3 days of annealing. These studies strongly suggest that the thickness of the SAN midlayer determines whether a blend resides in regime A or F. Namely, if the midlayer is too thin, the SAN dewets, whereas if it is thick a stable trilayer structure can be supported.

To quantify the trilayer stability associated with regimes A and F (cf. Figure 3), we propose a free energy model that attributes dewetting to capillary fluctuations at the PMMA/SAN interface.⁴³ In prior studies, we considered fluctuations in PMMA/SAN/PMMA to describe film stability.^{9–11} Here, we expand this approach to include the air and substrate contributions, namely, air/PMMA/SAN/PMMA/Si, where the PMMA layers have the same thickness, $h_{\text{PMMA}} = \phi_{\text{PMMA}} d/2$ and the SAN thickness is $h_{\text{SAN}} = (1 - \phi_{\text{PMMA}})d$. Using nonretarded long-range van der Waals forces, the free energy for the top and bottom PMMA/SAN interfaces are

$$G(d, \phi_{\text{PMMA}}) = -\frac{1}{12\pi} \left[\frac{A_{\text{PMMA/SAN/PMMA}}}{h_{\text{SAN}}^2} + \frac{A_{\text{air/PMMA/SAN}}}{h_{\text{PMMA}}^2} \right] \quad (\text{top}) \quad (5)$$

$$G(d, \phi_{\text{PMMA}}) = -\frac{1}{12\pi} \left[\frac{A_{\text{PMMA/SAN/PMMA}}}{h_{\text{SAN}}^2} + \frac{A_{\text{SAN/PMMA/Si}}}{h_{\text{PMMA}}^2} \right] \quad (\text{bottom}) \quad (6)$$

where $A_{a/b/c}$ is the Hamaker constant between a/b and b/c interfaces, which are separated by medium b .⁴⁴ In our study, contributions of silicon oxide ($\sim 2 \text{ nm}$) and short-range interactions can be safely neglected because d ranges from 50 to

hundreds of nm.⁴⁵ The Hamaker constants can be estimated from the dc dielectric constants and refractive indices of each medium. For air/PMMA/SAN, PMMA/SAN/PMMA, and SAN/PMMA/Si interfaces, the values are 1.4×10^{-21} , -8.31×10^{-21} , and $2.2 \times 10^{-20} \text{ J}$, respectively, where positive values denote attractive interactions between interfaces.⁴⁴ Because interfacial fluctuations are stable when $(d^2 G/dh_{\text{SAN}}^2) < 0$, fluctuations at the top interface are suppressed because of the repulsive interaction between air and SAN separated by the PMMA layer. However, fluctuations at the bottom SAN/PMMA interface grow in amplitude and eventually rupture the SAN layer. According to a liquid/liquid dewetting theory, the critical time to initiate film rupture is a strong function of SAN-layer thickness ($\tau_{\text{rupture}} \propto h_{\text{SAN}}^\delta$, $5 \leq \delta \leq 6$).^{46,47} Therefore, the thicker films associated with regime A are stable over a long time ($> 72 \text{ h}$), whereas the thinner films in regime F exhibit dewetting patterns in the SAN midlayer.

3.4. Perspective and Remarks. Our understanding of wetting and phase separation in polymer blend films has evolved rapidly over the past 10 years and is now ready to be applied to commercial systems.⁴⁸ The present study will greatly assist with this transition because it elucidates the mechanism of pattern development in polymer blend films as a function of composition and thickness and then summarizes the results in an easy-to-use morphology map to guide selection of desired morphologies. In this subsection, we present several unresolved issues and suggest the next generation of studies on wetting and phase separation in polymer blend films.

First, the stability of a buried liquid layer sandwiched between another liquid (i.e., A/B/A trilayer) requires both theoretical and experimental studies. This subject is of great practical interest because organic light-emitting devices (OLEDs) and field-effect transistors (FETs) are based on the layer-by-layer (LBL) deposition of polymers or organic molecules. These devices and transistors are limited by their stability upon heating.⁴⁹ In this work, studies of regimes A and F suggest (1) a possible one-step pathway to fabricate a self-organizing trilayer that is more straightforward than LBL and (2) guidelines to analyze the stability of devices prepared by LBL. For devices based on multiple coexisting components, film instability is more complicated because lateral composition variations due to phase separation can dominate, as recently pointed out by Clarke,² and demonstrated in our studies of regimes B, C, and D. Furthermore, interfacial roughening caused by phase separation⁵⁰ is unable to explain the multiple wavelength fluctuations ubiquitous to multilayer systems.^{10,11,48,51} At present, a minimization of interfacial energy argument⁷ is unable to explain the mechanism of film rupture. Thus, the stability of polymer blend films, as well as liquid multilayers, remains an open question requiring further study.

Second, self-organization and patterning of semiconducting polymer blend films has attracted tremendous attention because blending allows a one-step method to fabricate electronic devices such as PLEDs or photovoltaics.⁵² Moons has recently published an excellent review of the relationship between film morphology and the performance of PLEDs and photovoltaics.⁵³ In particular, a large interfacial area between phases is highly desirable for photovoltaic devices because excitons generated by light are readily dissociated at the interface. The challenge to preparing such devices is that n-type and p-type polymers are highly incompatible, and therefore, during spin-coating the blends undergo phase separation and wetting.^{54,55} Thus, the morphology map constructed in this study may provide important guidelines for selecting film thickness and composition to produce bicon-

tinuous morphologies desired to produce high-performance semiconducting devices.

Finally, polymer blend films containing nanoparticles, such as quantum dots, nanotubes, nanorods, and biological precursors, have just begun to receive significant attention. In particular, the optical, mechanical, and thermal properties of polymers can be improved by adding a low concentration of nanoparticles, and relevant to this study, the ultimate physical properties will be dictated by structural patterns.⁵⁶ The marriage between self-regulated pattern formation in polymer blend films and self-assembly of directed nanoparticles has the potential to revolutionize the performance of polymeric coatings. However, our understanding of the bulk or thin film phase behavior of blends containing nanoparticle is quite limited.^{57–60} Recently, we have found that nanoparticles can be directed into a particular phase, resulting in a slowdown of pattern development during the intermediate stage.⁴¹ For nanoparticles that partition to the interface between phases, patterns are pinned during the early and the intermediate stages, depending on nanoparticle concentration and film thickness.⁶¹ In conclusion, studies of polymer blend films containing nanoparticle are at its infancy, and their thermodynamic and dynamic behavior is not yet understood. The addition of nanoparticles also imparts new control over properties by varying particle type, size, surface chemistry, and shape.

4. Conclusion

In this study, a morphology map was created on the basis of the distinct morphology pathways displayed by PMMA:SAN blends during the intermediate stage. This map shows how variations in film thickness, 50–1000 nm, and PMMA volume fraction, 0.3–0.8, leads to six distinct pattern development regimes. As noted before, PMMA wets both the air and oxide interfaces. For films thicker than 80 nm and $\phi_{\text{PMMA}} = 0.4$ –0.7, the midlayer exhibits circular PMMA domains ($SF > 0.8$), elongated PMMA domains ($0.4 < SF < 0.8$), and bicontinuous PMMA/SAN domains ($SF < 0.4$) as a function of increasing ϕ_{PMMA} , which corresponds to regimes B, C, and D, respectively. This is the first time that the shape factor was used to distinguish between regimes in polymer blend films. For $\phi_{\text{PMMA}} = 0.8$, the SAN midlayer breaks into isolated droplets, leading to a stable film in regime E. In regime F, thinner films ($d < 80$ nm) initially form PMMA/SAN/PMMA trilayer structures and then roughen upon dewetting of the SAN midlayer. In regime A, thicker films ($d \geq 190$ nm) with $\phi_{\text{PMMA}} = 0.3$ also develop a trilayer structure, but in this case the trilayer is stable for 72 h at 185 °C. This study of pattern development mechanisms will serve as a guideline to control morphology shape and feature size, which are both critical design parameters for technological applications including organic devices and membranes.

Acknowledgment. We thank Ms. Ayşenur Çorlu (Koç University) for trilayer dewetting experiments. This work was financially supported by the National Science Foundation MRSEC (DMR05-20020) and Polymer (DMR02-34903) programs.

References and Notes

- (1) Binder, K. *Adv. Polym. Sci.* **1999**, *138*, 1–89.
- (2) Clarke, N. *Eur. Phys. J. E* **2004**, *14*, 207–210.
- (3) Straub, W.; Bruder, F.; Brenn, R.; Krausch, G.; Bielefeldt, H.; Kirsch, A.; Marti, O.; Mlynek, J.; Marko, J. F. *Europhys. Lett.* **1995**, *29*, 353–358.
- (4) Sung, L.; Karim, A.; Douglas, J. F.; Han, C. C. *Phys. Rev. Lett.* **1996**, *76*, 4368–4371.
- (5) Muller-Buschbaum, P.; Gutmann, J. S.; Stamm, M. *Macromolecules* **2000**, *33*, 4886–4895.
- (6) Heier, J.; Kramer, E. J.; Revesz, P.; Battistig, G.; Bates, F. S. *Macromolecules* **1999**, *32*, 3758–3765.
- (7) Hoppe, H.; Heuberger, M.; Klein, J. *Phys. Rev. Lett.* **2001**, *86*, 4863–4866.
- (8) Wang, H.; Composto, R. J. *Europhys. Lett.* **2000**, *50*, 622–627.
- (9) Wang, H.; Composto, R. J. *J. Chem. Phys.* **2000**, *113*, 10386–10397.
- (10) Wang, H.; Composto, R. J.; Hobbie, E. K.; Han, C. C. *Langmuir* **2001**, *17*, 2857–2860.
- (11) Wang, H.; Composto, R. J. *Macromolecules* **2002**, *35*, 2799–2809.
- (12) Wang, H.; Composto, R. J. *Interface Sci.* **2003**, *11*, 237–248.
- (13) Zhang Newby, B.-M.; Wakabayashi, K.; Composto R. J. *Polymer* **2001**, *42*, 9155–9162.
- (14) Chung, H.-J.; Composto R. J. *Phys. Rev. Lett.* **2004**, *92*, 185704.
- (15) Affrossman, S.; Jerome, R.; O'Neill, S. A.; Schmitt, T.; Stamm, M. *Macromolecules* **1996**, *29*, 5010–5016.
- (16) Tanaka, K.; Takahara, A.; Kajiyama, T. *Macromolecules* **1996**, *29*, 3232–3239.
- (17) Tsai, I. Y.; Kimura, M.; Russell, T. P. *Langmuir* **2004**, *20*, 5952–5957.
- (18) Raczkowska, J.; Rysz, J.; Budkowski, A.; Lekki, J.; Lekka, M.; Bernasik, A.; Kowalski, K.; Czuba, P. *Macromolecules* **2003**, *36*, 2419–2427.
- (19) Dalnoki-Veress, K.; Forrest, J. A.; Stevens, J. R.; Dutcher, J. R. *Physica A* **1997**, *239*, 87–94.
- (20) Walheim, S.; Schaffer, E.; Mlynek, J.; Steiner, U. *Science* **1999**, *283*, 520–522.
- (21) Ade, H.; Winesett, D. A.; Smith, A. P.; Qu, S.; Ge, S.; Sokolov, J.; Rafailovich, M. H. *Europhys. Lett.* **1999**, *45*, 526–532.
- (22) Ton-That, C.; Shard, A. G.; Teare, D. O. H.; Bradley, R. H. *Polymer* **2001**, *42*, 1121–1129.
- (23) Wang, P.; Koberstein, J. T. *Macromolecules* **2004**, *37*, 5671–5681.
- (24) Walheim, S.; Boltau, M.; Mlynek, J.; Krausch, G.; Steiner, U. *Macromolecules* **1997**, *30*, 4995–5003.
- (25) Liao, Y.; Su, Z.; Ye, X.; Li, Y.; You, J.; Shi, T.; An, L. *Macromolecules* **2005**, *38*, 211–215.
- (26) Wang, H.; Composto, R. J. *Phys. Rev. E* **2000**, *61*, 1659–1663.
- (27) Zhang Newby, B.-M.; Composto R. J. *Macromolecules* **2000**, *33*, 3274–3282.
- (28) Russ, J. C. *The Image Processing Handbook*, 4th ed.; CRC Press: Boca Raton, FL, 2002.
- (29) Katzen, D.; Reich, S. *Europhys. Lett.* **1993**, *21*, 55–60.
- (30) Wagner, A. J.; Cates, M. E. *Europhys. Lett.* **2001**, *56*, 556–562.
- (31) Chin, J.; Coveney, P. V. *Phys. Rev. E* **2002**, *66*, 016303.
- (32) Osborn, W. R.; Swift, M. R.; Yeomans, J. M.; Banavar, J. R. *Phys. Rev. Lett.* **1995**, *75*, 4031–4034.
- (33) Wu, Y.; Alexander, F. J.; Lookman, T.; Chen, S. *Phys. Rev. Lett.* **1995**, *74*, 3852–3855.
- (34) Gunton, J. D.; San Miguel, M.; Sahni, P. S. In *Phase Transition and Critical Phenomena*; Domb, C., Lebowitz, J. L., Eds.; Academic Press: New York, 1983.
- (35) Binder, K.; Stauffer, D. *Phys. Rev. Lett.* **1974**, *33*, 1006–1009.
- (36) Furukawa, H. *Phys. Rev. A* **1985**, *31*, 1003–1008.
- (37) Tanaka, H. *J. Chem. Phys.* **1996**, *105*, 10099–10114.
- (38) Siggia, E. D. *Phys. Rev. A* **1979**, *20*, 595–605.
- (39) Haas, C. K.; Torkelson, J. M. *Phys. Rev. Lett.* **1995**, *75*, 3134–3137.
- (40) Tanaka, H. *Europhys. Lett.* **1993**, *24*, 665–671.
- (41) Chung, H.-J.; Taubert, A.; Deshmukh, R. D.; Composto, R. J. *Europhys. Lett.* **2004**, *68*, 219–225.
- (42) Scholten, E.; Sagis, L. M. C.; van der Linden, E. *Macromolecules* **2005**, *38*, 3515–3518.
- (43) Sferazza, M.; Heppenstall-Butler, M.; Cubitt, R.; Bucknall, D.; Webster, J.; Jones, R. A. L. *Phys. Rev. Lett.* **1998**, *81*, 5173–5176.
- (44) Israelachvili, J. N. *Intermolecular and Surface Forces*; Academic Press: London, 1991.
- (45) Seemann, R.; Herminghaus, S.; Jacobs, K. *Phys. Rev. Lett.* **2004**, *86*, 5534–5537.
- (46) Brochard-Wyart, F.; Daillant, J. *Can. J. Phys.* **1990**, *68*, 1084–1088.
- (47) Brochard-Wyart, F.; Martin, P.; Redon, C. *Langmuir* **1993**, *9*, 3682–3690.
- (48) Geoghegan, M.; Krausch, G. *Prog. Polym. Sci.* **2003**, *28*, 261–302.
- (49) Chua, L.-L.; Ho, P. K. H.; Siringhaus, H.; Friend, R. H. *Appl. Phys. Lett.* **2004**, *84*, 3400–3402.
- (50) Koblinski, P.; Kumar, S. K.; Maritan, A.; Koplik, J.; Banavar, J. R. *Phys. Rev. Lett.* **1996**, *76*, 1106–1109.
- (51) Yoo, P. J.; Lee, H. H. *Phys. Rev. Lett.* **2003**, *91*, 154502.
- (52) Caciagli, F.; Stoneham, M. J. *Phys.: Condens. Matter* **2002**, *14*, v9–v11.
- (53) Moons, E. J. *Phys.: Condens. Matter* **2002**, *14*, 12235–12260.
- (54) Kim, J.-S.; Ho, P. K. H.; Murphy, C. E.; Friend, R. H. *Macromolecules* **2004**, *37*, 2861–2871.
- (55) Chappell, J.; Lidzey, D. G.; Jukes, P. C.; Higgins, A. M.; Thompson, R. L.; O'Connor, S.; Grizzi, I.; Fletcher, R.; O'Brien, J.; Geoghegan, M.; Jones, R. A. L. *Nat. Mater.* **2003**, *2*, 616–620.

- (56) Schmidt, G.; Malwitz, M. M. *Curr. Opin. Colloid Interface Sci.* **2004**, 8, 103–108.
- (57) Balazs, A. C. *Curr. Opin. Colloid Interface Sci.* **1999**, 4, 443–448.
- (58) Zhang, Y.; Ge, S.; Tang, B.; Koga, T.; Rafailovich, M. H.; Sokolov, J.; Peiffer, D. G.; Li, Z.; Dias, A. J.; McElrath, K. O.; Lin, M. Y.; Satija, S. K.; Urquhart, S. G.; Ade, H.; Nguyen, D. *Macromolecules* **2001**, 34, 7056–7065.
- (59) Yurekli, K.; Karim, A.; Amis, E. J.; Krishnamoorti, R. *Macromolecules* **2003**, 36, 7256–7267.
- (60) Tanaka, H.; Lovinger, A. J.; Davis, D. D. *Phys. Rev. Lett.* **1994**, 72, 2581–2584.
- (61) Chung, H.-J.; Ohno, K.; Fukuda, T.; Composto, R. J. *Nano Lett.* **2005**, 5, 1878–1882.

MA051513Z